

# Optimized Carrier Extraction at Interfaces for 23.6% Efficient Tin–Lead Perovskite Solar Cells

**Shuaifeng Hu**

Kyoto University <https://orcid.org/0000-0003-1312-075X>

**Kento Otsuka**

Kyoto University

**Richard Murdey**

Kyoto University

**Tomoya Nakamura**

Kyoto University

**Minh Anh Truong**

Kyoto University

**Takumi Yamada**

Kyoto University

**Taketo Handa**

Kyoto University

**Kazuhiro Matsuda**

Toray Research Center, Inc.

**Kyohei Nakano**

RIKEN

**Atsushi Sato**

University of Tsukuba

**Kazuhiro Marumoto**

University of Tsukuba <https://orcid.org/0000-0001-9792-0775>

**Keisuke Tajima**

RIKEN Center for Emergent Matter Science <https://orcid.org/0000-0003-1590-2640>

**Yoshihiko Kanemitsu**

Institute for Chemical Research, Kyoto University <https://orcid.org/0000-0002-0788-131X>

**Atsushi Wakamiya** (✉ [wakamiya@scl.kyoto-u.ac.jp](mailto:wakamiya@scl.kyoto-u.ac.jp))

Kyoto University <https://orcid.org/0000-0003-1430-0947>

---

**Article**

**Keywords:** perovskite solar cells, carrier extraction, centimeter-scale devices

**Posted Date:** July 24th, 2021

**DOI:** <https://doi.org/10.21203/rs.3.rs-727823/v1>

**License:**  This work is licensed under a Creative Commons Attribution 4.0 International License.

[Read Full License](#)

---

**Version of Record:** A version of this preprint was published at Energy & Environmental Science on January 1st, 2022. See the published version at <https://doi.org/10.1039/D2EE00288D>.

## **Optimized Carrier Extraction at Interfaces for 23.6% Efficient Tin-Lead Perovskite Solar Cells**

Shuaifeng Hu,<sup>a</sup> Kento Otsuka,<sup>a</sup> Richard Murdey,<sup>a</sup> Tomoya Nakamura,<sup>a</sup> Minh Anh Truong,<sup>a</sup> Takumi Yamada,<sup>a</sup> Taketo Handa,<sup>a</sup> Kazuhiro Matsuda,<sup>b</sup> Kyohei Nakano,<sup>c</sup> Atsushi Sato,<sup>d</sup> Kazuhiro Marumoto,<sup>d</sup> Keisuke Tajima,<sup>c</sup> Yoshihiko Kanemitsu,<sup>a</sup> Atsushi Wakamiya<sup>\*,a</sup>

<sup>a</sup>*Institute for Chemical Research, Kyoto University, Gokasho, Uji, Kyoto 611-0011, Japan.*

<sup>b</sup>*Surface Science Laboratories, Toray Research Center, Inc., 3-3-7, Sonoyama, Otsu, Shiga 520-8567, Japan.*

<sup>c</sup>*RIKEN Center for Emergent Matter Science (CEMS), Wako, Saitama 351-0198, Japan.*

<sup>d</sup>*Division of Materials Science, University of Tsukuba, Tsukuba, Ibaraki 305-8573, Japan.*

## **Abstract**

Carrier extraction is a key issue which limits the efficiency of perovskite solar cells. In this work, carrier extraction is improved by modifying the perovskite layers with a combination of ethylenediammonium diiodide post-treatment and glycine hydrochloride additive. Ethylenediammonium dications primarily affect the top surface of the perovskite films, while glycinium cations preferentially accumulate at the bottom region. The top and bottom interface modifications improve the crystallinity of the perovskite films and lower the density of electrical traps via surface passivation effects, resulting in long charge carrier lifetimes. The orientated aggregation of the ethylenediammonium and glycinium cations at the charge collection interfaces result in the formation of surface dipoles, which facilitate charge extraction. The performance of the treated solar cell devices also increases. The fill factor rose to 0.82, and the power conversion efficiency reaches 23.6% (23.1% certified). The open circuit voltage reaches 0.91 V, just 0.06 V below the Shockley–Queisser limit. The unencapsulated devices also show improved stability under AM 1.5G, retaining over 80% of the initial efficiency after 200 h continuous operation in inert atmosphere. Our strategy is also successfully applied to centimeter-scale devices, with efficiencies up to 21.0%.

## Introduction

Due to their strong optical absorption, tunable bandgap, and efficient charge generation<sup>1,2</sup>, metal halide perovskites are promising materials for printable, cost effective next-generation photovoltaics. The power conversion efficiency (PCE) of perovskite solar cells (PSCs) can be optimized for solar radiation by bringing the perovskite bandgap closer to the ideal range of 1.1–1.4 eV<sup>3,4</sup>. Although most lead perovskite materials have bandgaps larger than 1.45 eV<sup>5,6</sup>, smaller bandgaps can be obtained with tin–lead (Sn–Pb) compositions, where about half of the lead ions are substituted with tin<sup>7</sup>. Introducing tin into the perovskite lattice, however, can adversely affect the device performance<sup>8–10</sup> – primarily by self-doping due to the oxidation of Sn(II) to Sn(IV). This process readily occurs through reactions with the solvent<sup>11,12</sup> or trace oxygen<sup>13,14</sup>. Suppressing these oxidation processes is therefore the key to realizing high device performance. Several means have been reported to reduce the Sn(IV) content in tin-containing perovskite films, including reducing agents, such as hypophosphorous acid<sup>15</sup>, hydrazine vapor<sup>16</sup>, Sn powders<sup>17</sup> and nanoparticles<sup>18</sup>, and phenylhydrazine hydrochloride<sup>19</sup>, as well as antioxidants, including hydroquinone sulfonic acid<sup>20</sup>, gallic acid<sup>21</sup>, and ascorbic acid<sup>22</sup>.

By successfully suppressing oxidation processes, the highest PCE of Sn–Pb devices has reached 21.7%<sup>23,24</sup>. Xiao et al. achieved this by using a zwitterionic antioxidant, formamidine sulfonic acid, as a bifunctional additive, which both suppressed Sn(II) oxidation and passivated defects at the perovskite grain surfaces<sup>23</sup>. Tong et al. were able to passivate structural defects in Sn–Pb perovskite by adding guanidinium thiocyanate, which increased the charge carrier lifetimes ( $>1 \mu\text{s}$ ) and diffusion lengths ( $>2.5 \mu\text{m}$ )<sup>25</sup>. Meanwhile, very recently, we achieved ultra-long carrier lifetimes ( $>7 \mu\text{s}$ ) by applying a Sn(IV) scavenging method<sup>18</sup> and treating the purified Sn–Pb films with malto<sup>126</sup>. Even with these long lifetimes, however, the efficiencies of mixed Sn–Pb devices<sup>7,23–25,27–34</sup> still remain below those of their pure lead counterparts<sup>35–39</sup>. As the quality of the material already appears to sufficiently high, we believe that the efficiency of Sn–Pb PSCs is now primarily limited by poor carrier dynamics at the interfaces with the charge collection layers.<sup>40</sup> We therefore

aim to improve the structural and electronic properties at the top and bottom regions of the perovskite films by modifying them with surfactants containing methylammonium terminal groups.

### **Design strategy**

Methylammonium surfactants with different functional groups such as  $\text{NH}_3^+-\text{CH}_2-\text{R}$ ;  $\text{R} = -\text{CH}_2-\text{NH}_3^+$ , (Ethylenediammonium,  $\text{EDA}^{2+}$ ) or  $-\text{COOH}$ , (Glycinium,  $\text{GlyH}^+$ ) offer the means to systematically tailor the electrostatics at perovskite interfaces (Fig. 1a). The challenge is to find methods to selectively and reliably apply particular surfactant molecules to specific charge extraction surfaces.

Ethylenediammonium diiodide ( $\text{EDAI}_2$ ) can be coated onto the top surface of the perovskite layer by post-treatment. The ethylenediammonium dication ( $\text{EDA}^{2+}$ ) is sufficiently small to allow for electronic contact between the perovskite and the top charge transport layer (Fig. 1a). In addition, since  $\text{EDA}^{2+}$  is too short to occupy two A-sites of the perovskite lattice simultaneously<sup>41,42</sup>, two-dimensional phases should not be formed. We speculate that one methylammonium group of  $\text{EDA}^{2+}$  binds to the surface of the perovskite films, reducing the density of structural defects and unsatisfied dangling bonds. The other methylammonium group would then point away from the perovskite surface, inducing a surface dipole<sup>43</sup>, which may facilitate electron extraction from the top surface into the electron collecting layer of positive-intrinsic-negative (p-i-n) structured (inverted) PSCs.

When glycine hydrochloride ( $\text{GlyHCl}$ ) is added into the precursor solution used to prepare the perovskite films, the methylammonium head of  $\text{GlyH}^+$  is expected to bind to the surface of the perovskite crystallites. When these crystallites accumulate at the bottom interface, the electronegative carboxyl group will face outwards from the perovskite surfaces, towards the hole collection layer. The orientation of the surface dipole creates an electric field, which assists in driving the holes to the hole collection layer.

### **Realizing the modifications to the top and bottom regions**

We started with a triple-cation mixed Sn–Pb perovskite,  $\text{Cs}_{0.1}\text{FA}_{0.6}\text{MA}_{0.3}\text{Pb}_{0.5}\text{Sn}_{0.5}\text{I}_3$ , (MA = methylammonium, FA = formamidinium), fabricated, as reported in our previous work<sup>26</sup>, from a 1.8 M precursor solution prepared in *N,N*-dimethylformamide and dimethyl sulfoxide with a volume ratio of 3:1. 10 mol% tin fluoride ( $\text{SnF}_2$ ), with respect to  $\text{SnI}_2$ , and 2 mol% ammonium thiocyanate ( $\text{NH}_4\text{SCN}$ ), with respect to the total amount of B-site precursor ( $\text{SnI}_2 + \text{PbI}_2$ ), were added to the perovskite precursor solution.  $\text{SnF}_2$  suppresses Sn(II) oxidation<sup>18</sup>, while thiocyanate salts mediate the perovskite crystal growth<sup>7,44</sup>. This perovskite is the control to which the treated perovskite layers are compared. For top interface modification, a solution of  $\text{EDA}\text{I}_2$  in isopropanol/toluene (volume ratio of 1:1) is spin-coated on the top of perovskite films. This perovskite will be referred to as “ $\text{EDA}\text{I}_2$ -treated”. To modify the bottom interface, GlyHCl (2 mol% with respect to the total amount of B-site precursor) is added into the precursor solution. The perovskite layer to which both  $\text{EDA}\text{I}_2$  and GlyHCl treatments have been applied will be referred to as “ $\text{EDA}\text{I}_2$ /GlyHCl-treated”.

To pinpoint the regions affected by each treatment, time-of-flight secondary-ion mass spectrometry (ToF-SIMS) was used to track the distributions of the  $\text{EDA}^{2+}$  and  $\text{GlyH}^+$  ions throughout the perovskite film (Fig. S1–4). The ToF-SIMS results show that the  $\text{EDA}^{2+}$  cations introduced by the post-treatment are mainly distributed on the perovskite top surface (Fig. 1b, c). In contrast,  $\text{GlyH}^+$  cations are found to be mainly located at the bottom region of the perovskite films (Fig. 1b, c).

Further experiments were performed to better understand why  $\text{GlyH}^+$  cations preferentially aggregate towards the bottom region of the perovskite films (Fig. S5–15). Although it has been reported for ionic liquid additives that the concentration gradients in perovskite layers can depend on the substrates, such as  $\text{NiO}_x/\text{FTO}$ <sup>45</sup> and poly-TPD/FTO<sup>46</sup>, we found that the distribution of  $\text{GlyH}^+$  in the perovskite layers was not affected by whether the substrate was PEDOT:PSS-coated or bare FTO (Fig. S8–10). It therefore seems that the concentration gradients of  $\text{GlyH}^+$  cations are determined by dynamic forces within the perovskite intermediate during the crystallization and

growth phase (Fig. 1a), rather than by substrate-induced interactions.

### **Effects of the treatments on film quality**

The morphology of the perovskite layers was examined with scanning electron microscopy (SEM) and atomic force microscopy (AFM). All samples show good coverage with large grains. Post-treatment with the EDAl<sub>2</sub> solution appears to have a polishing effect<sup>47</sup>, washing away the surface layer of the perovskite film. In the control sample, some deposits, probably from SnF<sub>2</sub>, are visible between the grain boundaries (Fig. 1d). These deposits are less prominent after the perovskite films are post-treated with EDAl<sub>2</sub> solution, and the surface roughness is reduced from 42 nm for control to 37 nm for the films treated with EDAl<sub>2</sub> solution (Fig. S16).

Viewed in cross section, all the perovskite films show evenly-sized, monolithic grain structure. The film thickness is 870, 830, and 860 nm for the control, EDAl<sub>2</sub>-treated, and the EDAl<sub>2</sub>/GlyHCl-treated films, respectively (Fig. 1e). The EDAl<sub>2</sub>-treated film is notably thinner than the control, confirming the polishing effect of the post-treatment with EDAl<sub>2</sub> solution. The isopropanol/toluene co-solvent system was found to be critical for this top surface modification. The details are given in the supplementary information.

The effect of the treatments on the crystallinity of the perovskite layers was monitored by thin film X-ray diffraction (XRD) measurements (Fig. S17, S18). Peaks at 14.2°, 20.1°, 24.6°, 28.4°, 31.9°, 35.0°, 40.7°, and 43.2°, were observed for all the films, corresponding to (100), (110), (111), (200), (210), (211), (220), and (300) planes, respectively. The intensity of the (100) peak increases after the EDAl<sub>2</sub> post-treatment, possibly as a result of the surface polishing effect<sup>47</sup> and/or second stage crystallization<sup>48</sup>. The intensity of the (100) peak was enhanced further in the spectra of the EDAl<sub>2</sub>/GlyHCl-treated film, suggesting that the GlyHCl additive enhances the crystallinity of the film at the crystal growth stage. The small peak at  $2\theta = 12.7^\circ$  is attributed to PbI<sub>2</sub> from unreacted precursor material or degraded perovskite. Although the peak was observed in the patterns of the control and EDAl<sub>2</sub>-treated films, it was absent in that of the EDAl<sub>2</sub>/GlyHCl-treated perovskite film.

For effective charge extraction, high quality perovskite films with long charge carrier lifetimes are necessary. The improvements in the carrier dynamics were evaluated by using steady-state photoluminescence (PL) and time-resolved PL (TRPL). The excitation energy was 1.80 eV, and the excitation photon flux was fixed at  $3.5 \times 10^{11}$  photons  $\text{cm}^{-2}$  ( $100 \text{ nJ cm}^{-2}$ ), comparable to the incident photon flux under AM 1.5G. The perovskite films were excited either from the top surface of the perovskite film (front-side, Fig. S19), or through the quartz substrate (back-side, Fig. 2a, b). Regional sampling specificity is possible, since the thickness of the perovskite films ( $\sim 850 \text{ nm}$ ) is considerably greater than the estimated optical penetration depth ( $1/\alpha$ :  $\sim 220 \text{ nm}$ ,  $\alpha$  is absorption coefficient at 688 nm, Fig. S20). In each condition, a single PL peak around 1.24 eV was observed, with PL lifetimes on the order of microseconds. With front-side excitation, the lifetime increased from  $2.8 \mu\text{s}$  for the control films, to  $4.5 \mu\text{s}$  for the  $\text{EDA}\text{I}_2$  post-treated films, and  $4.9 \mu\text{s}$  for the  $\text{EDA}\text{I}_2/\text{GlyHCl}$ -treated films, indicating that defects are greatly suppressed. At the top surface, most of the improvement originates from the  $\text{EDA}\text{I}_2$  treatment, as expected. Meanwhile, with back-side excitation, the lifetimes were elongated from  $1.5 \mu\text{s}$  for control sample, to  $3.2 \mu\text{s}$  for  $\text{EDA}\text{I}_2$ -treated, and finally to  $5.5 \mu\text{s}$  for the  $\text{EDA}\text{I}_2/\text{GlyHCl}$ -treated films. Notably, the influence of the GlyHCl on the lifetimes is more prominent when the bottom region is probed. The steady state PL intensities were also increased (Table S1, Fig. S21). The results clearly show that  $\text{EDA}\text{I}_2$  post-treatment and GlyHCl additive are able to reduce the density of recombination centers in the  $\text{EDA}\text{I}_2/\text{GlyHCl}$ -treated perovskite films, particularly at the top and bottom regions, respectively<sup>49</sup>.

In order to better characterize the photocarrier recombination dynamics in the  $\text{EDA}\text{I}_2/\text{GlyHCl}$ -treated films, the PL decay was examined under different excitation intensities. The dependencies of PL decay curves, PL lifetimes, and initial PL intensities on photon flux are shown in Fig. 2c, d, S22. The decay curves can be modelled with the rate equations reported in our previous work<sup>50</sup>. The results indicate that bimolecular recombination is dominant under a photon flux equivalent of AM 1.5G (initial carrier density  $n_0 = 1.5 \times 10^{16} \text{ cm}^{-3}$ ). The charge carrier trapping rate is  $9.2 \times 10^4 \text{ s}^{-1}$ , three orders of magnitude lower than that of prototypical metal halide perovskite  $\text{MAPbI}_3$ <sup>50</sup>. The

low trap densities for both electrons and holes are confirmed by space-charge-limited current (SCLC) measurements (Fig. S23, Table S2). Most of these traps can be reasonably assumed to be located at the various surfaces of the perovskite layer<sup>51</sup>. From the decay curve fits, the charge carrier density from unintentional doping is estimated to be  $8.2 \times 10^{14} \text{ cm}^{-3}$ , a value similar to the carrier densities reported for lead perovskite films ( $\sim 10^{15} \text{ cm}^{-3}$ )<sup>50</sup>.

To summarize, the EDAl<sub>2</sub>/GlyHCl-treated perovskite films, modified with both EDAl<sub>2</sub> surface treatment and with the addition of GlyHCl, show improved crystallinity and reduced defect densities, especially at the top and bottom regions. The characteristic p-doping, commonly observed in Sn-containing perovskite materials, has been effectively suppressed.

### Solar cell performance

The cells had the following inverted architecture: Fluorine-doped tin oxide (FTO)/poly(3,4-ethylenedioxythiophene): poly(styrene sulfonate) (PEDOT:PSS)/perovskite/fullerene (C<sub>60</sub>)/bathocuproine (BCP)/silver (Ag) (Fig. 3a). The active cell area was 0.0985 cm<sup>2</sup>. Current density–voltage (*J–V*) curves were measured under simulated AM 1.5G illumination (Fig. 3b). The best performance of the control cells was 19.6% (Reverse scan,  $V_{OC} = 0.79 \text{ V}$ ,  $J_{SC} = 31.6 \text{ mA cm}^{-2}$ , and FF = 0.79). After the EDAl<sub>2</sub> post-treatment, the PCE increased to 21.7% (Reverse scan,  $V_{OC} = 0.85 \text{ V}$ ,  $J_{SC} = 32.3 \text{ mA cm}^{-2}$ , and FF = 0.79). The FF remains the same, but the  $J_{SC}$  and  $V_{OC}$  increased. For the EDAl<sub>2</sub>/GlyHCl-treated device, a maximum PCE of 23.6% was obtained (Reverse scan,  $V_{OC} = 0.89 \text{ V}$ ,  $J_{SC} = 32.5 \text{ mA cm}^{-2}$ , and FF = 0.82). The *J–V* curves of the EDAl<sub>2</sub>/GlyHCl-treated devices also show lower hysteresis, suggesting suppressed ion movements<sup>52</sup>. In addition to the increase in  $V_{OC}$ , the FF improved as well. This efficiency is the highest reported value for any Sn–Pb perovskite solar cell, as well as being the highest reported value for any PSC having an inverted structure (Fig. S24). The certified cell performance from a third-party institution was 23.1% ( $V_{OC} = 0.88 \text{ V}$ ,  $J_{SC} = 32.5 \text{ mA cm}^{-2}$ , and FF = 0.81) (Fig. S25, S26). The *J–V* results are summarized in Fig. S27 and Table S3.

The external quantum efficiency (EQE) and internal quantum efficiency (IQE) spectra are shown in Fig. 3c. The highest IQE is close to unity, and the EQE reached 90%. The integrated  $J_{sc}$  from the EQE spectrum is  $32.2 \text{ mA cm}^{-2}$ , in close agreement with the values derived from the  $J-V$  scans ( $32.5 \text{ mA cm}^{-2}$ ). The bandgap, estimated from the inflection point of the EQE spectrum<sup>53</sup>, is 1.24 eV, in close agreement with the PL results.

As the effective device area is larger than optical mask used for the  $J-V$  measurements, the recorded  $V_{oc}$  values are slightly underestimated. With the mask removed, the  $V_{oc}$  reached 0.91 V (Fig. 3d), 0.06 V below the thermodynamic limit of 0.97 V<sup>54</sup>. This corresponds to a voltage loss of 0.33 V – one of the best results thus far for perovskite devices<sup>35,55</sup>. The low voltage loss together with the long charge carrier lifetimes observed in the PL experiments confirm the remarkable suppression of non-radiative recombination channels in the EDAI<sub>2</sub>/GlyHCl-treated devices.

The operational stability was evaluated by tracking the maximum power point (MPP) under AM 1.5G. Unencapsulated devices were measured in a N<sub>2</sub>-filled glovebox. The EDAI<sub>2</sub>/GlyHCl-treated cell maintained over 80% of the initial PCE for up to 200 h, and was more stable than either the EDAI<sub>2</sub>-treated (65% in 180 h) or control (60% in 145 h) cells (Fig. 3e, S28).

Our top and bottom interface modification strategy was also applied to the fabrication of larger, centimeter-scale PSCs (Table S4, Fig. S29, S30). For 1 cm<sup>2</sup> active area, a champion PCE of 21.0% (Forward scan,  $V_{oc} = 0.88 \text{ V}$ ,  $J_{sc} = 33.1 \text{ mA cm}^{-2}$ , and FF = 0.72) was achieved. The cells generally showed minimal hysteresis and good reproducibility.

### **Carrier extraction**

For further insights regarding the improved performance, especially the low voltage loss, the effect of the EDAI<sub>2</sub> and GlyHCl treatments on the energy levels of the perovskite films was examined with ultraviolet photoemission spectroscopy (UPS). The UPS experiments probe the vacuum, Fermi, and valence energy levels near the top surface of the perovskite films, where electrons are extracted in the working solar cells.

Four systems were measured. In addition to the control and EDAl<sub>2</sub> post-treated samples, the films with GlyHCl additive with and without EDAl<sub>2</sub> post-treatment were examined. With this sample set, we investigated the influence of the EDAl<sub>2</sub> post-treatment on the perovskite films prepared both without, and with, GlyHCl additive. The secondary electron cutoffs, from which the work function of the perovskite surface can be estimated as  $(21.22 \text{ eV} - E_{B,\text{max}})$ , are shown in Fig 4a. The onset of the valence band relative to the Fermi level is estimated from the spectral data in Fig. 4b. The energy of the Fermi and vacuum levels for each of the four samples relative to the valence band maximum (VBM) and conduction band minimum (CBM) are compiled in Fig 4c. Comparing the control and EDAl<sub>2</sub>-treated films, we can see that the vacuum level and Fermi levels both shift, by 0.05 eV and 0.11 eV, respectively, to lie closer to the CBM. When the perovskite film contains GlyHCl additive, however, the shift in Fermi level is less pronounced, at only 0.02 eV, while the EDAl<sub>2</sub> post-treatment results in a shift in vacuum energy of 0.04 eV, similar to what was observed for the control films.

In the UPS measurements, a surface dipole is indicated by a change of the vacuum level ( $E_{\text{vac}}$ ) relative to the valence level of the perovskite films (Fig. 4c, S31, S32)<sup>43</sup>. Post-treatment with EDAl<sub>2</sub> leads to the formation of a surface dipole with a magnitude of about 0.05 eV for the control film, and 0.04 eV for the film fabricated with GlyHCl additive. The positive end of the dipole faces outwards from the perovskite<sup>35,56</sup>. These results support our hypothesis that the EDA<sup>2+</sup>, which accumulates at the top surface, is collectively bound to, and oriented at, the perovskite crystal grains. The potential difference created by the dipole can facilitate electron extraction by helping to sweep electrons away from the perovskite surface and towards the C<sub>60</sub> electron collection layer<sup>56</sup>.

In addition, electron extraction may be enhanced by surface doping effects, indicated by the shifts of the UPS-determined Fermi levels ( $E_F$ ) with respect to the valence and conduction bands. EDAl<sub>2</sub> post-treatment appears to induce the perovskite surface to become more n-type (the  $E_F$  shifts to lie above the center of the band gap, Fig. 4c). The shift is more pronounced for the control film than the film with GlyHCl additive, at  $-0.11 \text{ eV}$  vs.  $-0.02 \text{ eV}$ , respectively. The result can be

understood by noting that while the Fermi level of the control film was nominally at the middle of the bandgap (0.60 eV from the VBM), the Fermi level of the GlyHCl-treated film was already close to the conduction band (0.71 eV from the VBM). Thus, while EDAL<sub>2</sub> post-treatment makes the perovskite surface more n-type, the effect appears to vary depending on how p-type the surface region was initially. The Fermi level shifts correlate well with the difference in Sn(IV) concentrations observed by X-ray photoelectron spectroscopy (XPS, Fig. S33, Table S5). If the top surface is more n-type than the bulk, band bending will be induced in the downwards direction at the perovskite, facilitating electron extraction by drawing electrons to, and holes away from, the extraction layer.

As GlyH<sup>+</sup> cations mainly accumulate at the bottom region of the perovskite films, electron spin resonance (ESR) spectroscopy was used to examine the charge extraction from the perovskite layers to the PEDOT:PSS substrate. The ESR signal allows us to quantify the charge states in PEDOT:PSS films with and without perovskite capping layers (Fig. 4d, S34, Table S6). The unit intensity is the peak-to-peak ESR intensity of the Mn<sup>2+</sup> standard sample ( $I_{Mn}$ ). The ESR absorption intensity of the PEDOT:PSS film was 131  $I_{Mn}$  units, centered at 319.2 mT. When the PEDOT:PSS layer was coated with the control perovskite, the absorption intensity of the PEDOT:PSS ESR signal decreased to 63.6  $I_{Mn}$  units, indicating that, as a result in the difference in Fermi levels between the perovskite layer and the PEDOT:PSS<sup>57</sup>, some electrons from perovskite recombine with holes in the PEDOT:PSS layer at the interface. When the PEDOT:PSS is coated with the perovskite containing GlyHCl additive, however, the absorption intensity is only reduced to 85.6  $I_{Mn}$  units, indicating fewer recombination events.

The change in absorption intensity of the ESR signal correlates with the relative position of the Fermi levels in the PEDOT:PSS and perovskite layers. The results imply that the Fermi level in the PEDOT:PSS and perovskite layers are closer in energy when GlyHCl additive is used. The UPS results, meanwhile, confirm that the work function of the perovskite layer is not evidently altered by the addition of GlyHCl (control: 4.73 eV, GlyHCl: 4.69 eV). The GlyH<sup>+</sup> cation, which

accumulates at the bottom interface, binds to, and aligns with, the perovskite crystal face (Fig. 1a, 4e), inducing a surface dipole where the electronegative  $-\text{COOH}$  group points outwards from the perovskite surface. The resulting dipole, with the negative side facing the PEDOT:PSS layer, creates an electric field which drives the holes to PEDOT:PSS (Fig. 4e)<sup>58</sup>.

## Conclusions

Mixed Sn–Pb solar cells with high open circuit voltages and high fill factors were realized by optimizing charge extraction. Interface modification strategies using surfactants containing methylammonium terminal groups were used to facilitate the extraction of electrons and holes at the top and bottom perovskite surfaces, respectively. Post-treatment with  $\text{EDA}_2$  showed polishing and passivation effects at the top surface, leading to lower carrier trap densities. GlyHCl additive resulted in the accumulation of  $\text{GlyH}^+$  cations at the bottom region of the perovskite layer as well as an improvement in film crystallinity. The GlyHCl treatment helped to passivate recombination centers, particularly at the bottom region of the perovskite layer. In addition to improvements to the perovskite layer,  $\text{EDA}^{2+}$  and  $\text{GlyH}^+$  cations at the top and bottom regions induced surface dipoles which facilitates electron and hole transfer, respectively, to the charge collection layers.

As a result of the improvements arising from the top and bottom passivation and dipole formation, the PCE of mixed Sn–Pb solar cells with  $0.0985 \text{ cm}^2$  aperture area increased to 23.6% (certified 23.1%), the highest value reported so far for mixed Sn–Pb PSCs, and the highest value reported so far for PSCs with the inverted structure regardless of perovskite composition. Our top and bottom interface modification strategy was also applied to the fabrication of larger, centimeter-scale PSCs showing high efficiency with small hysteresis and good reproducibility. The approach should be widely applicable to other perovskite semiconductor devices, such as all-perovskite and perovskite/silicon tandem photovoltaics, perovskite light-emitting diodes, transistors, and X-ray detectors.

## REFERENCES AND NOTES:

- 1 Stranks, S. D. & Snaith, H. J. Metal-halide perovskites for photovoltaic and light-emitting devices. *Nat. Nanotechnol.* **10**, 391–402 (2015).
- 2 Nayak, P. K., Mahesh, S., Snaith, H. J. & Cahen, D. Photovoltaic solar cell technologies: analysing the state of the art. *Nat. Rev. Mater.* **4**, 269–285 (2019).
- 3 Leng, K., Fu, W., Liu, Y., Chhowalla, M. & Loh, K. P. From bulk to molecularly thin hybrid perovskites. *Nat. Rev. Mater.* **5**, 482–500 (2020).
- 4 Shockley, W. & Queisser, H. J. Detailed balance limit of efficiency of p–n junction solar cells. *J. Appl. Phys.* **32**, 510–519 (1961).
- 5 Eperon, G. E. *et al.* Formamidinium lead trihalide: a broadly tunable perovskite for efficient planar heterojunction solar cells. *Energy Environ. Sci.* **7**, 982–988 (2014).
- 6 Hui, W. *et al.* Stabilizing black-phase formamidinium perovskite formation at room temperature and high humidity. *Science* **371**, 1359 (2021).
- 7 Klug, M. T. *et al.* Metal composition influences optoelectronic quality in mixed-metal lead–tin triiodide perovskite solar absorbers. *Energy Environ. Sci.* **13**, 1776–1787 (2020).
- 8 Ke, W., Stoumpos, C. C. & Kanatzidis, M. G. “Unleaded” perovskites: Status quo and future prospects of tin-based perovskite solar cells. *Adv. Mater.* **31**, 1803230 (2019).
- 9 Cao, J. P. & Yan, F. Recent progress in tin-based perovskite solar cells. *Energy Environ. Sci.* **14**, 1286–1325 (2021).
- 10 Euvrard, J., Yan, Y. & Mitzi, D. B. Electrical doping in halide perovskites. *Nat. Rev. Mater.* **6**, 531–549 (2021).
- 11 Saidaminov, M. I. *et al.* Conventional solvent oxidizes Sn(II) in perovskite inks. *ACS Energy Lett.* **5**, 1153–1155 (2020).
- 12 Pascual, J. *et al.* Origin of Sn(II) oxidation in tin halide perovskites. *Mater. Adv.* **1**, 1066–1070 (2020).
- 13 Noel, N. K. *et al.* Lead-free organic–inorganic tin halide perovskites for photovoltaic

- applications. *Energy Environ. Sci.* **7**, 3061–3068 (2014).
- 14 Hao, F., Stoumpos, C. C., Cao, D. H., Chang, R. P. H. & Kanatzidis, M. G. Lead-free solid-state organic–inorganic halide perovskite solar cells. *Nat. Photonics* **8**, 489–494 (2014).
- 15 Li, W. *et al.* Additive-assisted construction of all-inorganic CsSnIBr<sub>2</sub> mesoscopic perovskite solar cells with superior thermal stability up to 473 K. *J. Mater. Chem. A* **4**, 17104–17110 (2016).
- 16 Song, T.-B. *et al.* Importance of reducing vapor atmosphere in the fabrication of tin-based perovskite solar cells. *J. Am. Chem. Soc.* **139**, 836–842 (2017).
- 17 Lin, R. *et al.* Monolithic all-perovskite tandem solar cells with 24.8% efficiency exploiting comproportionation to suppress Sn(II) oxidation in precursor ink. *Nat. Energy* **4**, 864–873 (2019).
- 18 Nakamura, T. *et al.* Sn(IV)-free tin perovskite films realized by in situ Sn(0) nanoparticle treatment of the precursor solution. *Nat. Commun.* **11**, 3008 (2020).
- 19 Wang, C. *et al.* Illumination durability and high-efficiency Sn-based perovskite solar cell under coordinated control of phenylhydrazine and halogen ions. *Matter* **4**, 709–721 (2021).
- 20 Tai, Q. *et al.* Antioxidant grain passivation for air-stable tin-based perovskite solar cells. *Angew. Chem. Int. Ed.* **58**, 806–810 (2019).
- 21 Wang, T. *et al.* Highly air-stable tin-based perovskite solar cells through grain-surface protection by gallic acid. *ACS Energy Lett.* **5**, 1741–1749 (2020).
- 22 Xu, X. *et al.* Ascorbic acid as an effective antioxidant additive to enhance the efficiency and stability of Pb/Sn-based binary perovskite solar cells. *Nano Energy* **34**, 392–398 (2017).
- 23 Xiao, K. *et al.* All-perovskite tandem solar cells with 24.2% certified efficiency and area over 1 cm<sup>2</sup> using surface-anchoring zwitterionic antioxidant. *Nat. Energy* **5**, 870–880 (2020).
- 24 Kapil, G. *et al.* Tin-lead perovskite fabricated via ethylenediamine interlayer guides to the solar cell efficiency of 21.74%. *Adv. Energy Mater.* **11**, 2101069 (2021).

- 25 Tong, J. *et al.* Carrier lifetimes of  $>1 \mu\text{s}$  in Sn–Pb perovskites enable efficient all-perovskite tandem solar cells. *Science* **364**, 475 (2019).
- 26 Hu, S. *et al.* Mixed lead–tin perovskite films with  $>7 \mu\text{s}$  charge carrier lifetimes realized by maltol post-treatment. *Submitted* (2021).
- 27 Kapil, G. *et al.* Strain relaxation and light management in tin–lead perovskite solar cells to achieve high efficiencies. *ACS Energy Lett.* **4**, 1991–1998 (2019).
- 28 Yang, Z. *et al.* Enhancing electron diffusion length in narrow-bandgap perovskites for efficient monolithic perovskite tandem solar cells. *Nat. Commun.* **10**, 4498 (2019).
- 29 Wei, M. *et al.* Combining efficiency and stability in mixed tin–lead perovskite solar cells by capping grains with an ultrathin 2D layer. *Adv. Mater.* **32**, 1907058 (2020).
- 30 Ke, W. *et al.* Narrow-bandgap mixed lead/tin-based 2D Dion–Jacobson perovskites boost the performance of solar cells. *J. Am. Chem. Soc.* **142**, 15049–15057 (2020).
- 31 Li, C. *et al.* Low-bandgap mixed tin–lead iodide perovskites with reduced methylammonium for simultaneous enhancement of solar cell efficiency and stability. *Nat. Energy* **5**, 768–776 (2020).
- 32 Prasanna, R. *et al.* Design of low bandgap tin–lead halide perovskite solar cells to achieve thermal, atmospheric and operational stability. *Nat. Energy* **4**, 939–947 (2019).
- 33 Tong, J. *et al.* High-performance methylammonium-free ideal-band-gap perovskite solar cells. *Matter* **4**, 1365–1376 (2021).
- 34 Ruggeri, E. *et al.* Controlling the growth kinetics and optoelectronic properties of 2D/3D lead–tin perovskite heterojunctions. *Adv. Mater.* **31**, 1905247 (2019).
- 35 Li, F. *et al.* Regulating surface termination for efficient inverted perovskite solar cells with greater than 23% efficiency. *J. Am. Chem. Soc.* **142**, 20134–20142 (2020).
- 36 Yoo, J. J. *et al.* Efficient perovskite solar cells via improved carrier management. *Nature* **590**, 587–593 (2021).
- 37 Alsalloum, A. Y. *et al.* 22.8%-Efficient single-crystal mixed-cation inverted perovskite

- solar cells with a near-optimal bandgap. *Energy Environ. Sci.* **14**, 2263–2268 (2021).
- 38 Jeong, J. *et al.* Pseudo-halide anion engineering for  $\alpha$ -FAPbI<sub>3</sub> perovskite solar cells. *Nature* **592**, 381–385 (2021).
- 39 Wu, S. *et al.* 2D metal–organic framework for stable perovskite solar cells with minimized lead leakage. *Nat. Nanotechnol.* **15**, 934–940 (2020).
- 40 Xue, J., Wang, R. & Yang, Y. The surface of halide perovskites from nano to bulk. *Nat. Rev. Mater.* **5**, 809–827 (2020).
- 41 Li, X., Hoffman, J. M. & Kanatzidis, M. G. The 2D halide perovskite rulebook: how the spacer influences everything from the structure to optoelectronic device efficiency. *Chem. Rev.* **121**, 2230–2291 (2021).
- 42 Han, Y. *et al.* From distortion to disconnection: linear alkyl diammonium cations tune structure and photoluminescence of lead bromide perovskites. *Adv. Opt. Mater.* **8**, 1902051 (2020).
- 43 Quarti, C., De Angelis, F. & Beljonne, D. Influence of surface termination on the energy level alignment at the CH<sub>3</sub>NH<sub>3</sub>PbI<sub>3</sub> perovskite/C<sub>60</sub> interface. *Chem. Mater.* **29**, 958–968 (2017).
- 44 Zhang, H. *et al.* Synergistic effect of anions and cations in additives for highly efficient and stable perovskite solar cells. *J. Mater. Chem. A* **6**, 9264–9270 (2018).
- 45 Bai, S. *et al.* Planar perovskite solar cells with long-term stability using ionic liquid additives. *Nature* **571**, 245–250 (2019).
- 46 Lin, Y.-H. *et al.* A piperidinium salt stabilizes efficient metal-halide perovskite solar cells. *Science* **369**, 96 (2020).
- 47 Lin, Y. Z. *et al.* Revealing defective nanostructured surfaces and their impact on the intrinsic stability of hybrid perovskites. *Energy Environ. Sci.* **14**, 1563–1572 (2021).
- 48 Xue, J. *et al.* Crystalline liquid-like behavior: surface-induced secondary grain growth of photovoltaic perovskite thin film. *J. Am. Chem. Soc.* **141**, 13948–13953 (2019).

- 49 Yang, Y. *et al.* Top and bottom surfaces limit carrier lifetime in lead iodide perovskite films. *Nat. Energy* **2**, 16207 (2017).
- 50 Yamada, Y., Nakamura, T., Endo, M., Wakamiya, A. & Kanemitsu, Y. Photocarrier recombination dynamics in perovskite  $\text{CH}_3\text{NH}_3\text{PbI}_3$  for solar cell applications. *J. Am. Chem. Soc.* **136**, 11610–11613 (2014).
- 51 Luo, D., Su, R., Zhang, W., Gong, Q. & Zhu, R. Minimizing non-radiative recombination losses in perovskite solar cells. *Nat. Rev. Mater.* **5**, 44–60 (2020).
- 52 Zhang, W. *et al.* Revealing the role of bifunctional molecules in crystallizing methylammonium lead iodide through geometric isomers. *Chem. Mater.* **33**, 4014–4022 (2021).
- 53 Krückemeier, L., Rau, U., Stolterfoht, M. & Kirchartz, T. How to report record open-circuit voltages in lead-halide perovskite solar cells. *Adv. Energy Mater.* **10**, 1902573 (2020).
- 54 Rühle, S. Tabulated values of the Shockley–Queisser limit for single junction solar cells. *Sol. Energy* **130**, 139–147 (2016).
- 55 Jeong, M. *et al.* Stable perovskite solar cells with efficiency exceeding 24.8% and 0.3-V voltage loss. *Science* **369**, 1615 (2020).
- 56 Zhang, M. *et al.* Reconfiguration of interfacial energy band structure for high-performance inverted structure perovskite solar cells. *Nat. Commun.* **10**, 4593 (2019).
- 57 Gotanda, T. *et al.* Direct observation of charge transfer at the interface between PEDOT:PSS and perovskite layers. *Appl. Phys. Express* **12**, 041002 (2019).
- 58 Ansari, F. *et al.* Passivation mechanism exploiting surface dipoles affords high-performance perovskite solar cells. *J. Am. Chem. Soc.* **142**, 11428–11433 (2020).

### **Acknowledgements:**

This work was partially supported by JST–ALCA (JPMJAL 1603), JST–COI (JPMJCE 1307), and JST–CREST (JPMJCR 16N3) programs, NEDO, JST-Mirai Program, International Collaborative

Research Program of ICR, Kyoto University, ICR Grants for Promoting Integrated Research, Kyoto University, grants for the Integrated Research Consortium on Chemical Sciences, Tokyo Ohka Foundation for the Promotion of Science and Technology, Grant-in-Aid for Research Activity Start-up (20K22531), Grant-in-Aid for Early-Career Scientists (21K14694), Grant-in-Aid for Scientific Research (C) (19K05666) and Grant-in-Aid for Scientific Research (A) (21H04699), JSPS for a Research Fellowship for Young Scientists (21J14762), and the China Scholarship Council (CSC). We thank Dr. Takayuki Yamamoto and Prof. Toshiyuki Nohira (Kyoto University) for XPS measurement, Dr. Masato Goto and Prof. Yuichi Shimakawa (Kyoto University) for XRD measurement, Dr. Kouji Nagashima and Prof. Kazuyuki Hirao (Kyoto University) for preliminary ToF-SIMS measurement, Dr. Katsuaki Suzuki (Kyoto University) and Prof. Hironori Kaji (Kyoto University) for the help of PLQY measurement. Kanagawa Institute of Industrial Science and Technology (KISTEC) for the measurement of device certification, Prof. Hideo Ohkita (Kyoto University), Kazuki Hata (Toray Research Center), and Tiancheng Tan (Kyoto University) for valuable discussion.

**Author contributions:**

S.H. conceived the idea. S.H. measured the SEM. R.M. performed AFM characterization. S.H. conducted the XRD measurement. K.M. conducted the ToF-SIMS measurement. S.H. and K.O. carried out the PL measurements with the help of T.Y., T.H., and Y.K. S.H. fabricated the solar cell devices and did the related characterizations. T.Y., T.H., and Y.K. analyzed the PL dynamics. S.H. conducted the XPS measurement with the help of M.A.T. M.A.T. and S.H. conducted the optical absorption measurement. K.N. and K.T. conducted the UPS measurement. S.H. conducted the SCLC measurements with the help of R.M. A.S. and K.M. conducted the ESR measurements. R.M. and S.H. performed the impedance measurement. T.N. and S.H. conducted the PLQY measurement. S.H., R.M., and A.W. prepared the manuscript. All authors commented on the manuscript. A.W. supervised the project.

**Competing interests:**

There are no conflicts to declare.

**Additional information** Extended data is available for this paper at <https://doi.org/XXXX>.

**Supplementary information** The online version contains supplementary material available at <https://doi.org/XXXX>.

**Correspondence and requests for materials** should be addressed to A.W.

**Peer review information** XXXX thanks XX and the other, anonymous, reviewer(s) for their contribution to the peer review of this work.

**Reprints and permissions information** is available at [www.nature.com/reprints](http://www.nature.com/reprints).

**Corresponding author**

\*E-mail: [wakamiya@scl.kyoto-u.ac.jp](mailto:wakamiya@scl.kyoto-u.ac.jp)

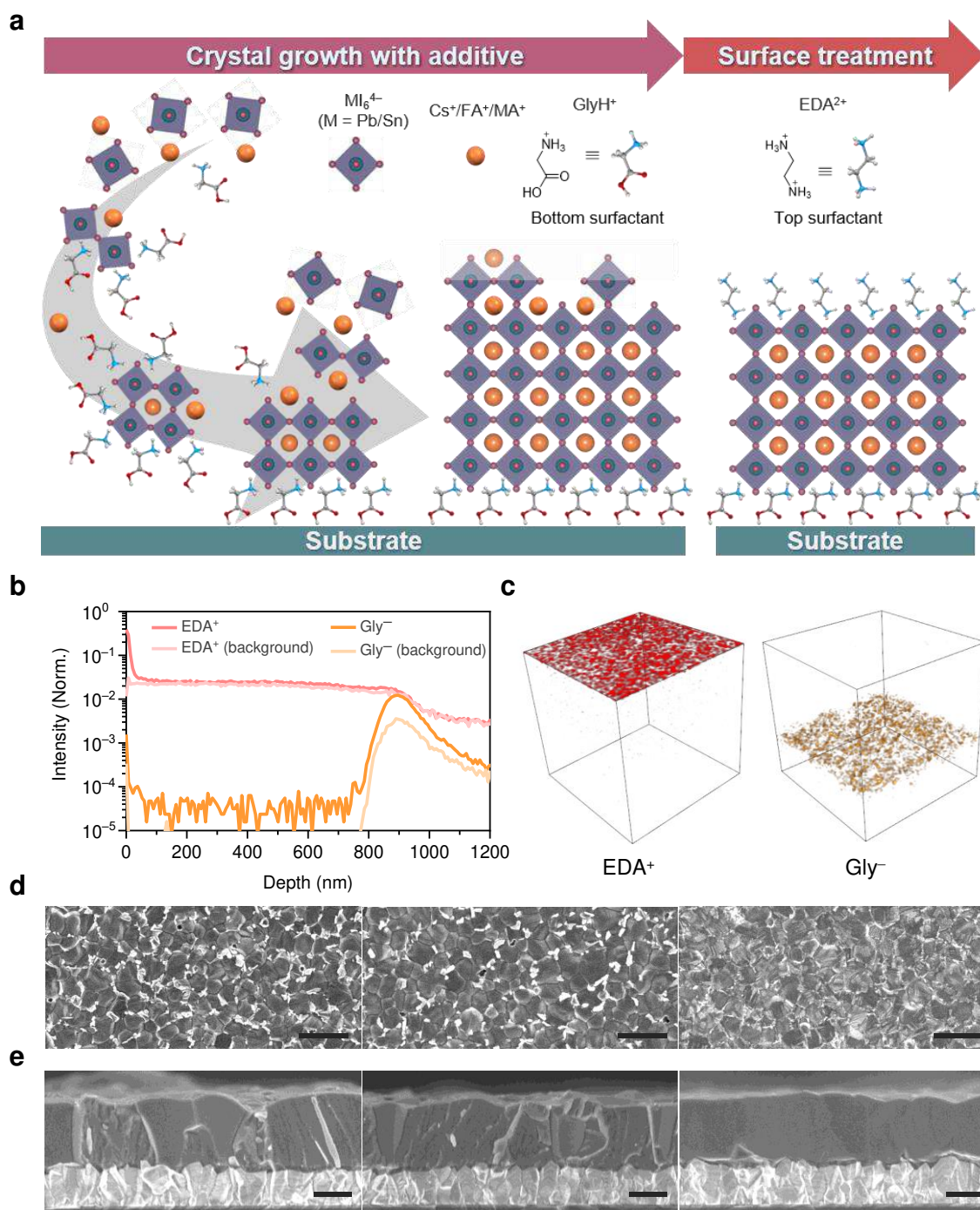


**Fig. 1** | Narrow-bandgap perovskite films with top and bottom interface modification. **a**, Schematic illustration of the interface modifications of mixed Sn–Pb perovskite films by GlyHCl additive and EDA<sub>2</sub> surface treatment. **b**, ToF-SIMS depth profile of EDA<sup>+</sup> and Gly<sup>-</sup> ions for the EDA<sub>2</sub>/GlyHCl-treated perovskite film on PEDOT:PSS/FTO. Full ion profiles are given in the

supplementary information (Fig. S1–15). **c**, Reconstructed, background subtracted 3D maps showing the distributions of  $\text{EDA}^+$  and  $\text{Gly}^-$  ions through the modified perovskite films. The raster area of the primary ion beam was  $30\ \mu\text{m}\times 30\ \mu\text{m}$ , and the thickness axis has been expanded for clarity. **d**, Top-view (scale bar:  $2\ \mu\text{m}$ ) and **e**, cross-sectional (scale bar:  $500\ \text{nm}$ ) SEM images of the control,  $\text{EDAI}_2$ -treated, and  $\text{EDAI}_2/\text{GlyHCl}$ -treated (left to right) perovskite films on PEDOT:PSS-coated FTO/glass substrates.

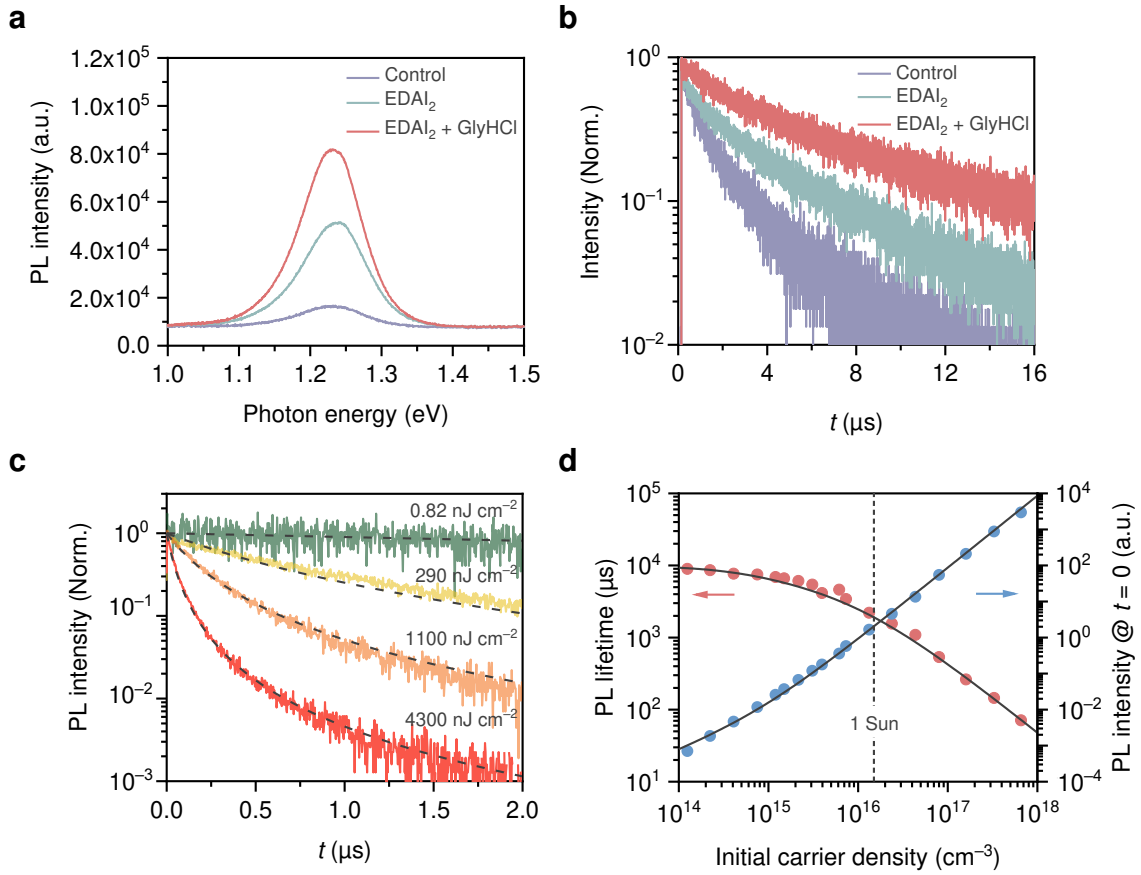


**Fig. 2 | Carrier dynamics.** **a**, Steady state photoluminescence (PL) spectra and **b**, time-resolved photoluminescence (TRPL) for the perovskite films on quartz substrates. **c**, PL decay curves for the EDAl<sub>2</sub>/GlyHCl-treated perovskite film showing the variation in PL lifetimes with excitation intensity. Curve fits used to ascertain the PL lifetimes<sup>50</sup> are shown by the dashed lines, see supplementary information (Fig. S22). **d**, Dependence of the lifetime and initial intensity of the PL signal on the excitation fluence. An initial carrier density of  $1.5 \times 10^{16} \text{ cm}^{-3}$  corresponds to an excitation fluence of  $100 \text{ nJ cm}^{-2}$  (approx. AM 1.5G, 1 Sun). Black solid lines are the curve fits obtained using the rate equations reported in our previous work<sup>50</sup>.

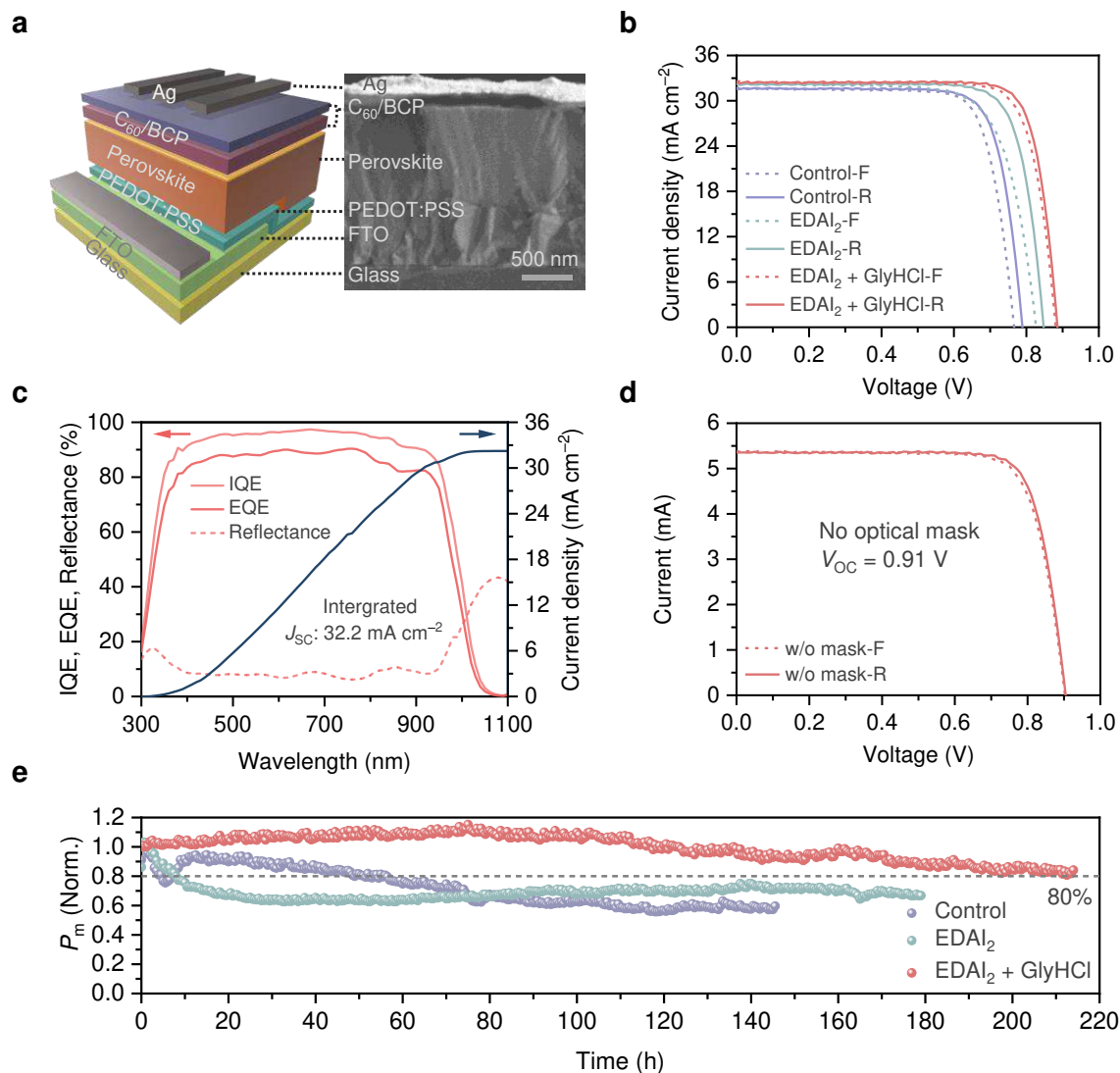


**Fig. 3| Solar cell devices.** **a**, Schematic and cross-sectional SEM image. **b**,  $J-V$  curves of the best performing devices. **c**, The EQE, IQE, and reflectance spectra of an EDAI<sub>2</sub>/GlyHCl-treated device. **d**,  $J-V$  curves for the champion device measured with no optical mask and an active area of 0.16 cm<sup>2</sup>. The open-circuit voltage is 0.91 V. **e**, Normalized maximum power point tracking (MPPT) curves for the unencapsulated control, EDAI<sub>2</sub>-treated, and EDAI<sub>2</sub>/GlyHCl-treated devices operating under AM 1.5G in inert atmosphere. The initial efficiencies were 14.8, 18.2, and 20.1%, respectively.

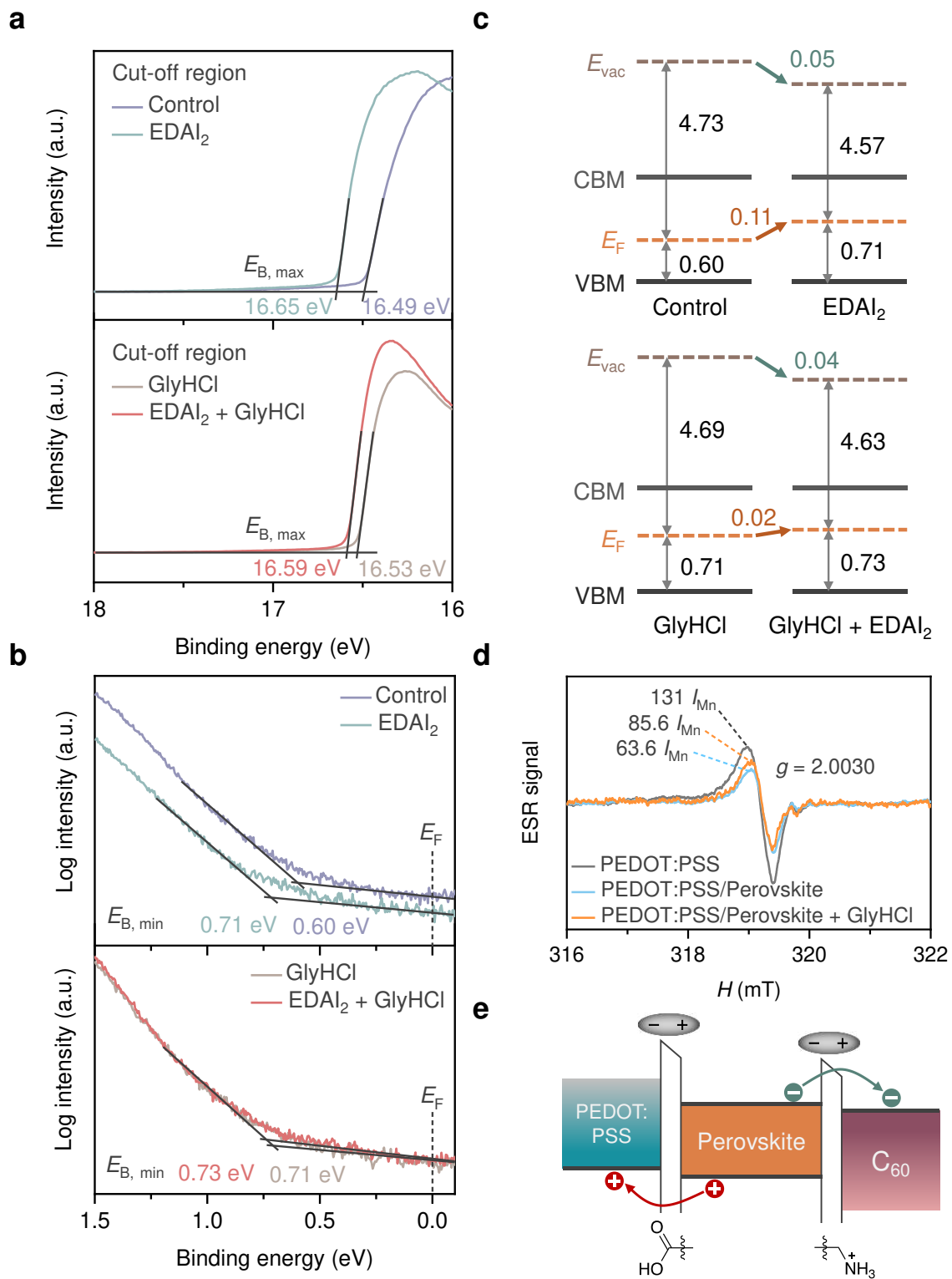


**Fig. 4| Band structure and surface dipole formation. a**, Secondary electron cut-off and **b**, valence band regions of the UPS spectra for the perovskite films. **c**, Energy-level scheme based on the

UPS spectra. The full analysis is shown in Fig. S30–31. Energy values are given in electron volts relative to the vacuum level,  $E_{\text{vac}}$ , and the conduction band energies are determined from the bandgap of 1.24 eV estimated from the PL measurements. **d**, The ESR spectra for PEDOT:PSS on quartz, with or without a perovskite capping layer. The  $g$ -factor is 2.0030. **e**, Schematic illustrating how electron and hole extraction may be enhanced by surface dipoles induced by  $\text{EDA}^{2+}$  and  $\text{GlyH}^+$  cations at the top and bottom perovskite interfaces, respectively.

## Supplementary Files

This is a list of supplementary files associated with this preprint. Click to download.

- [SISnPbPSCs.pdf](#)